Mapping of the spectral density function of a C^α-H^α bond vector from NMR relaxation rates of a ^{13}C-labelled α-carbon in motilin*

Peter Allard, Jüri Jarvet**, Anders Ehrenberg and Astrid Gräslund***

Department of Biophysics, Arrhenius Laboratories, Stockholm University, S-106 91 Stockholm, Sweden

Summary

The peptide hormone motilin was synthesised with a ^{13}C-enriched α-carbon in the leucine at position 10. In aqueous solution, six different relaxation rates were measured for the ^{13}C$^\alpha$-H$^\alpha$ fragment as a function of temperature and with and without the addition of 30% (v/v) of the cosolvent d_2-1,1,1,3,3,3-hexafluoro-2-propanol (HFP). The relaxation rates were analysed employing the spectral density mapping technique introduced by Peng and Wagner [(1992) *J. Magn. Reson.*, **98**, 308-332] and using the model-free approach by Lipari and Szabo [(1982) *J. Am. Chem. Soc.*, **104**, 4546-4570]. The fit to various models of dynamics was also considered. Different procedures to evaluate the overall rotational correlation time were compared. A single exponential time correlation function was found to give a good fit to the measured spectral densities only for motilin in 30% (v/v) HFP at low temperatures, whereas at high temperatures in this solvent, and in D$_2$O at all temperatures, none of the considered models gave an acceptable fit. A new empirical spectral density function was tested and found to accurately fit the experimental spectral density mapping points. The application of spectral density mapping based on NMR relaxation data for a specific ^{13}C-^{1}H vector is shown to be a highly useful method to study biomolecular dynamics. Advantages are high sensitivity, high precision and uniform sampling of the spectral density function over the frequency range.

Introduction

Motilin is a gastrointestinal peptide hormone consisting of 22 amino acids (Poitras, 1994). Porcine motilin has the sequence FVPIF$_5$TYGEL$_{10}$QRMQE$_{15}$KERNK$_{20}$GQ and, with a single ^{13}C label, a molecular mass of 2698 Da. The first eight amino-terminal residues are mostly hydrophobic, while the rest of the peptide can be considered to be hydrophilic in nature.

Motilin can be found in blood and in some endocrine cells in the gut. Its primary function appears to be regulation of the migrating motor complex. Membrane-bound receptors have been found in the smooth muscle of the duodenum. The antibiotic erythromycin has motilin-like activity and can displace motilin from its receptor (Kondo et al., 1988).

The secondary structure of motilin in 30% (v/v) HFP has previously been determined using NMR (Khan et al., 1990). The three-dimensional structure was later calculated from the same NOESY data using distance geometry, followed by restrained molecular dynamics and finally an iterative relaxation matrix approach (Edmondson et al., 1991). The refined structure can be described by two types of secondary structure. The hydrophobic

---

amino terminus is an ill-defined turn while an α-helix spans the hydrophilic sequence from Glu[9] to Lys[20]. No crystal structure of motilin has been reported.

The effects of different solvents on the structure and dynamics of motilin have been studied with circular dichroism (Backlund et al., 1994) and time-resolved fluorescence (TFD) using Tyr[7] as an intrinsic fluorescence probe (Backlund et al., 1995).

^{13}C NMR relaxation is a unique method allowing the spectroscopist to study the overall and internal mobility of peptides and proteins in their native state in solution. The spectral density mapping technique, proposed by Peng and Wagner (1992a,b), opens the possibility to obtain all available information from the relaxation experiments in the form of spectral densities. The relaxation of α-carbons in a polypeptide chain is well defined. The dipole–dipole relaxation mechanism is dominating and the relaxation of the α-carbons occurs almost exclusively via the directly bound α-proton. Only glycine, which has two α-protons, needs a different approach because of its A_2X spin system (Daragan and Mayo, 1992). By using the α-protons for excitation and detection of α-carbon resonances, the experimental sensitivity is greatly enhanced compared with direct detection, allowing the spectroscopist to perform more experiments in a shorter time. The use of selective ^{13}C labelling with inverse detection makes it possible to perform ^{13}C NMR relaxation experiments for studies of molecular mobility with comparable or even higher information content than in the case of time-resolved fluorescence experiments.

In the present study, we have used the relaxation of a [13]C-^{1}H pair in Leu[10] of porcine motilin for detailed studies of the dynamics of the vector connecting the two nuclei. Both the effect of temperature and of addition of HFP to the solvent have been studied. The results, using different methods of evaluation, have been compared with each other and also with results from fluorescence experiments.

The ^{13}C label at Leu[10] is in the α-helical part of the molecule in 30% (v/v) HFP. The secondary structure determined under these conditions resembles the membrane-bound conformation of the peptide, with presumably the same part of the sequence in a stabilised helical conformation (Backlund et al., 1994). A maximum of α-helix content was obtained with 30% (v/v) HFP according to CD data (Khan et al., 1990). Taking the ellipticity at 222 nm as a measure of α-helix content, the amount of α-helix under these conditions is 50%, whereas in a pure aqueous sample it is 20%. It has not yet been possible to determine by NMR the secondary structure for Leu[10] in an aqueous sample without HFP added.

Theory

General theory

From the semiclassical NMR relaxation theory (Abra-

gam, 1962), it is seen that the relaxation rate of a certain coherence is determined by the generalised spectral density function and constants and coefficients that are dependent on the form of interaction causing relaxation. All information about dynamics is included in the spectral density function. The spectral density is a function of frequency, and its shape is a function of dynamics. The spectral density at certain frequencies affects the relaxation. For a two-spin system consisting of a proton and a carbon, the relevant frequencies for dipole–dipole relaxation are 0, ω_H, ω_C, $\omega_H - \omega_C$ and $\omega_H + \omega_C$. All types of relaxation rates are dependent on the spectral density at several of these frequencies.

The spectral density function is the Fourier cosine transform of the time-correlation function $G(\tau)$. The time-correlation function describes the decay of correlation of a single vector, as in the case of an auto-correlation function, or the decay of correlation between two vectors, as in the case of a cross-correlation function. Only the decay of the orientational auto-correlation function caused by rotational diffusion and internal motion will be considered in this study.

A model that describes the motion of the relevant vector is necessary in order to extract relevant information about dynamics from relaxation data. Many such models exist and analytical expressions for spectral densities that contain physically meaningful parameters are available.

For the interpretation of NMR relaxation results it has been common to directly include analytical expressions for the spectral density into the relaxation rate equations. During the last decade, the most popular way to do this has been using the so-called model-free approach (Lipari and Szabo, 1982a,b). This model assumes that the motion can be described by two correlation times on different time scales. The two fundamental assumptions made in this model are that the fast and slow motions are statistically independent and that the slow motion is isotropic. If this is true, the fast motion can be described by a generalised order parameter S, which is a measure of the spatial restriction of the motion, and a correlation time τ_e, which is a measure of the rate of motion. The slow isotropic motion corresponds to the overall rotational correlation time τ_m for the molecule.

The spectral density mapping method, proposed by Peng and Wagner (1992a,b) for an [1]H-X vector, where X is a spin 1/2 heteronucleus, is a true model-free approach for the study of dynamics using a set of NMR relaxation experiments. By the measurement of a total of six different relaxation rates, it is possible to calculate the spectral density at the five relevant frequencies and also to determine a sixth parameter, the contribution to the longitudinal relaxation rate of the proton bound to nucleus X, caused by other protons. The great advantage of this approach is that it enables separation of the measurement of spectral densities from the fitting of motional models.

Sources of systematic errors

Since the C^α-H^α fragment is not isolated from the influence of surrounding nuclei, there are various contributions that may decrease the accuracy of the measured relaxation rates. The contribution of dipolar interactions from neighbouring protons to α-carbon relaxation rates has usually been neglected, as its influence was considered to be small. For gramicidin-S the contribution to relaxation from exchangeable protons to C^α relaxation has been experimentally determined to be about 1–2% and ascribed to the C^α-NH interaction (Rossi et al., 1991). Calculating interatomic distances from the available Protein Data Bank coordinate files of peptides and proteins and assuming that these distances are relevant in the relaxation processes, we have found that the contribution from neighbouring protons to the relaxation rate of $^{13}C^\alpha$ usually is in the range of 5 to 7%, whereas for the backbone amide ^{15}N, the corresponding value is 3 to 4%. In the present case, the directly bound α-proton at a distance of 1.09 Å will certainly dominate the relaxation of the α-carbon, but the two β-protons at distances of 2.11 and 2.15 Å, determined from structural coordinates obtained by NMR, and the amide proton at a distance of 2.55 Å, will together give a contribution to the relaxation rate of about 5%, the exact amount depending on internal dynamics and the type of relaxation process. The contribution of β-protons and other, not directly bound, protons might be taken into account as a fictitious decrease of the effective distance r_{eff}:

$$r_{eff}^{-6} = r_{C^\alpha-H^\alpha}^{-6} + r_{C^\alpha-H^\beta}^{-6} + r_{C^\alpha-H^{\beta'}}^{-6} + r_{C^\alpha-H^N}^{-6} + \sum_i r_{C^\alpha-H^i}^{-6}$$

neglecting cross terms in the relaxation and assuming that spectral density functions of other proton–carbon vectors do not differ much from that of the C^α-H^α vector. This assumption is justified when the overall dynamics, which is common to all nuclei in the molecule, is dominating the relaxation. With this assumption and taking the C^α-H^α distance to be 1.090 Å, the effective distance becomes r_{eff} = 1.079 Å. In the present case we might expect vectors to the neighbouring protons to be more affected by local motion than the C^α-H^α vector itself. This means that the estimated value of r_{eff} is a lower limit. This decrease of effective distance by about 1% corresponds to an increase in relaxation rates of about 6%. For ^{13}C, this effect of neighbouring protons on the relaxation rates has been of the same order as the experimental accuracy of the determined rates, when relaxation rates were determined at the natural abundance level of ^{13}C.

We use a synthesised motilin peptide, labelled with ^{13}C in the α-carbon of Leu[10]. The α-carbons of the other 21 amino acid residues in motilin, with ^{13}C at natural abundance, also give a small contribution to the intensity of 1D spectra due to spectral overlap. Their dynamical parameters should be close to those of the labelled residue.

Hence, the influence on the measured rates and calculated spectral densities may be neglected.

At higher magnetic fields, relaxation caused by the anisotropy of shielding becomes more effective. With a typical chemical shift anisotropy $\Delta\delta$ of 25 ppm for α-carbons (Palmer et al., 1991 and references cited therein), the contribution to relaxation by chemical shift anisotropy will be about 1% at a magnetic field of 9.4 T.

For the following evaluation we have neglected all these sources of systematic errors. The shape of the spectral density function is to a first-order approximation not very sensitive to the exact value of the distance r_{eff}. Other systematic errors that may affect the measured relaxation rates will be considered in the discussion of deviations between the mapped spectral densities and existing dynamical models.

Materials and Methods

Peptide synthesis

The peptide was manually synthesised using a stepwise *tert*-butyloxycarbonyl (*tert*-Boc) solid phase synthesis. The *tert*-Boc amino acids were activated using 2-(1H-benzotriazole-1-yl)-1,1,3,3-tetramethyluronium tetrafluoroborate (TBTU) dissolved in a solution of N-hydroxybenzotriazole (HOBt) in dimethylformamide (DMF). A (*tert*-Boc)-Gln-OCH$_2$-phenylacetamidomethyl (PAM) resin (Applied Biosystems, Foster City, CA) was used to couple the second amino acid. After synthesis the peptide was deprotected with 50/50 (v/v) trifluoroacetic acid/dichloromethane and cleaved from the resin with hydrogen fluoride. Purification was performed by reversed phase HPLC (C$_{18}$ column 218-TP1022, Vydac). The purity was checked with analytical HPLC (C$_{18}$ column 218TP1010, Vydac). The correct molecular mass, 2698.5 Da, was confirmed by the experimentally determined mass of 2698.1 Da, using plasma desorption mass spectrometry (Model Bioion 20, Applied Biosystems).

Sample preparation

The HFP-containing NMR sample was prepared by dissolving 12.7 mg of lyophilised peptide in 60/10/30% (v/v/v) H$_2$O/D$_2$O/HFP. Deuterated acetic acid (20 mM) was used as buffer and the pH was adjusted to 3.9 using minute amounts of solid NH$_4$HCO$_3$. The peptide concentration was 7.1 mM, estimated using the molar extinction coefficient of tyrosine $\varepsilon_{274.6}$ = 1420 M^{-1} cm^{-1} (Wetlaufer, 1962). The sample in aqueous solution was prepared by dissolving the lyophilised peptide in D$_2$O. The UV-determined concentration in this case was 3.0 mM. The HFP-containing sample was stable, even close to the HFP boiling point of 58.2 °C. The aqueous sample started to precipitate at 55 °C.

NMR spectroscopy

All NMR experiments were performed on a JEOL

Alpha A400 spectrometer at a proton frequency of 399.78 MHz. A 5 mm sample tube, type 535-PP (Wilmad) and an inverse detection probe were used. All experiments were run as 1D sequences, by omitting the t_1 period from the corresponding 2D pulse sequences. The following parameters were used if no alternative values are stated. The recycle delay was 3 s, including a 1.5 s on-resonance DANTE (Morris and Freeman, 1978) water suppression pulse train (Zuiderweg et al., 1986). A J-coupling of 150 Hz was used for calculation of the delays in the INEPT steps (Morris and Freeman, 1979). A spectral width of 4000 Hz was used during acquisition and 256 complex points were sampled, resulting in a 64 ms acquisition time. Carbon decoupling during accumulation was accomplished using WALTZ-16 (Shaka et al., 1983) with a field strength of approximately 2.5 kHz. A total of 192 scans were added for each delay time τ and 16 dummy scans were used for each increment. In all experiments except in the NOE measurements, a nonequilibrium coherence is created and its monoexponential decay is followed by incrementation of a variable delay τ. Extremely good temperature stability is of crucial importance for the inversely detected experiments, since they are of the cancellation type. The best results were obtained using an external thermostat with the spectrometer temperature controller switched off. The sample temperature was calibrated using a thermocouple thermometer inserted into a sample tube.

Pulse sequences

The pulse sequences are presented graphically in Fig. 1. The symbols we will use (Peng and Wagner, 1992a) refer to specific relaxation rates $R_{OBS}(Q)$. Q is the type of coherence or population, the decay of which is to be probed, and 'OBS' refers to the nucleus or pair of nuclei whose relaxation is to be measured. According to this nomenclature, $R_C(C_z)$ is the carbon longitudinal relaxation rate, $R_C(C_{x,y})$ is the carbon in-phase transverse relaxation rate, $R_{CH}(2H_zC_z)$ is the relaxation rate of longitudinal two-spin order, also called dipolar order, $R_{CH}(2H_zC_{x,y})$ is the relaxation rate of carbon antiphase coherence and finally, $R_H(H_z)$ is the proton longitudinal relaxation rate. The pulse sequences to measure $R_C(C_z)$ and $R_C(C_{x,y})$ are essentially those of Barbato et al. (1992), while the $R_{CH}(2H_zC_z)$, $R_{CH}(2H_zC_{x,y})$ and $R_H(H_z)$ are essentially those described by Peng and Wagner (1992a).

The heteronuclear cross-relaxation rate was calculated using the steady-state $\{^1H\}$-^{13}C NOE and the measured carbon longitudinal relaxation rate $R_C(C_z)$. Two separate experiments were used to measure the intensity increase caused by the NOE. A total of 1024 scans were accumulated for both spectra. In the first experiment, with NOE enhancement, the protons were saturated with 2000 pulses using a pulse length of 120° and a pulse delay of 2 ms. The total NOE buildup time was 4 s, which is considered long enough to be complete. After the buildup of NOE

the carbon magnetization was transferred to the J-coupled proton using a refocused INEPT step (Burum and Ernst, 1980) and detected. In the reference spectra, water was suppressed at the end of the 4 s pulse delay with a water presaturation pulse of 50 ms. The buildup rate of the NOE as a function of the proton saturation time equals the carbon longitudinal relaxation rate (Kowalewski et al., 1978). The selective water suppression pulse is shorter than the carbon longitudinal relaxation time and causes only minor excitation at the α-proton frequency; it should therefore give a negligible NOE buildup. The rest of the pulse sequence is identical to the previous one.

The carbon longitudinal relaxation rate ($R_C(C_z)$) measurement starts with a refocused INEPT step from proton to carbon. The phase cycling used for the relaxation measurement will give a single exponential decay of magnetization to zero as a function of τ and can therefore be fitted with two parameters; it is not necessary to use three, as in the case of an inversion recovery experiment. This phase cycling will not introduce systematic errors, even if the delay between experiments is too short to allow carbon magnetization to relax completely (Sklenář et al., 1987). The protons are saturated during τ using a series of 90° pulses with 1 ms delay inbetween. The pulse train is surrounded by scramble pulses (Barbato et al., 1992) at full power for 2.5 ms. The proton decoupling will suppress cross relaxation between protons and carbon and help the cancellation of ^{12}C-bound protons, as well as improve water suppression. After the variable delay τ, the magnetization was transferred back to proton for detection. The τ values used were 20, 50, 80, 110, 140, 170, 200 and 230 ms.

The carbon transverse relaxation rate ($R_C(C_{x,y})$) measurement also begins and ends with refocused INEPT steps. A CPMG sequence was used during τ, with the time between refocusing pulses set to 2 ms in order to minimise development of antiphase coherence (Peng et al., 1991). Several different delays were used in order to make sure that the 2 ms delay corresponds to a minimum of the measured relaxation rate, so that the contribution to the rate from exchange is minimised. A proton 180° pulse was inserted between every second carbon refocusing pulse, to suppress cross correlation between CSA relaxation and dipolar relaxation (Kay et al., 1992; Palmer et al., 1992). This is not essential for a proton–carbon spin system, because of the small contribution from CSA relaxation, but was included anyway to improve water suppression. After the CPMG sequence, the carbon magnetization was stored along the z-axis. A hard 2.5 ms scramble pulse was then applied on the proton channel. The resulting inhomogeneity of the B_1 field will destroy most of the proton magnetisation. In this way, most importantly, the cancellation of protons bound to ^{12}C becomes much more effective and, in addition, the water suppression is improved. Moreover, fewer dummy scans
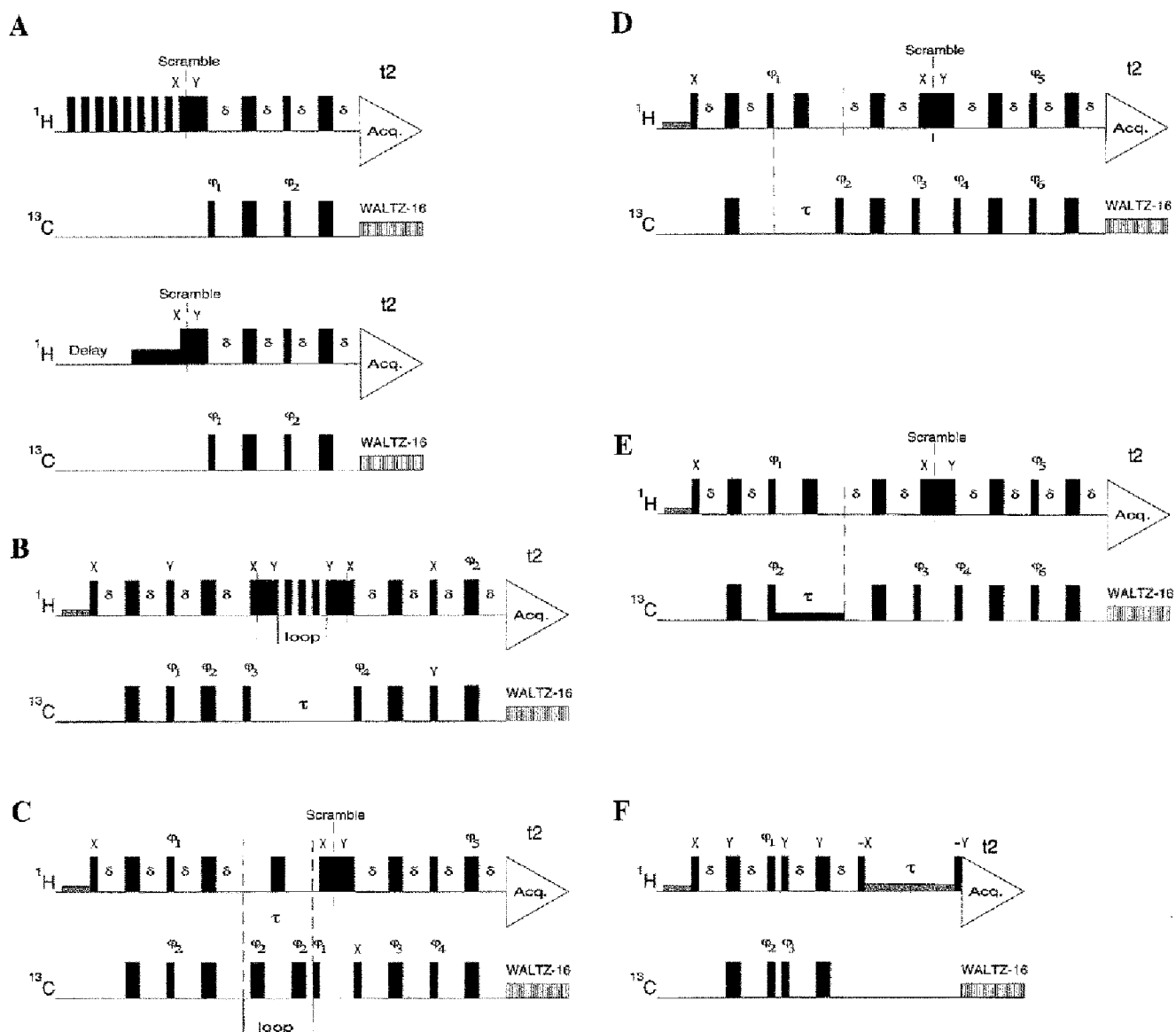
Fig. 1. Pulse sequences used for measuring the six relaxation parameters discussed in the text. The delay δ was set to $(4J)^{-1}$. The scramble pulses were 2.5 ms long and were applied at full power. The phase is x when no alternative is stated. (A) Steady-state NOE measurement: In the experiment with NOE enhancement, the protons were saturated with 2000 pulses using a pulse length of 120° and a pulse delay of 2 ms. In the reference spectra water was suppressed with a 50 ms water presaturation pulse, followed by scramble pulses: $\phi_1 = x,-x$; $\phi_2 = 2(y),2(-y)$; Acq. = x,-x,-x,x. (B) Carbon longitudinal relaxation rate $R_C(C_z)$ measurement: $\phi_1 = 4(x),4(-x)$; $\phi_2 = 8(x),8(y),8(-x),8(-y)$; $\phi_3 = y,-y$; $\phi_4 = 2(x),2(-x)$; Acq. = x,-x,-x,x,-x,x,x,-x. (C) Carbon transverse relaxation rate $R_C(C_{x,y})$ measurement: $\phi_1 = y,-y$; $\phi_2 = 2(x),2(-x)$; $\phi_3 = 16(x),16(-x)$; $\phi_4 = 8(y),8(-y)$; $\phi_5 = 4(x),4(y)$; Acq. = 2(x),4(-x),2(x),2(-x),4(x),2(-x). (D) Longitudinal two-spin order relaxation rate $R_{CH}(2H_zC_z)$ measurement: $\phi_1 = y,-y$; $\phi_2 = 2(y),2(-y)$; $\phi_3 = x,-x,-x,x$; $\phi_4 = x,-x$; $\phi_5 = 4(x),4(-x)$; $\phi_6 = 2(y),2(-y)$; Acq. = x,-x,-x,x,-x,x,x,-x. (E) Carbon antiphase relaxation rate $R_{CH}(2H_zC_{x,y})$ measurement: $\phi_1 = 2(y),2(-y)$; $\phi_2 = y,-y$; $\phi_3 = x,-x,-x,x$; $\phi_4 = x,-x$; $\phi_5 = 4(x),4(-x)$; $\phi_6 = 2(y),2(-y)$; Acq. = x,-x,-x,x,-x,x,x,-x. (F) Proton longitudinal relaxation rate $R_H(H_z)$ measurement: $\phi_1 = 4(y),4(-y)$; $\phi_2 = x,-x$; $\phi_3 = 2(x),2(-x)$; Acq. = x,-x,-x,x,-x,x,x,-x.

are needed to reach a steady-state condition. The suppression of protons bound to ^{12}C is especially important when using 1D spectra (as compared to 2D), because in 1D spectra the unwanted residual magnetization may overlap with the peaks of interest. The τ values used in the measurement were 16, 28, 40, 52, 64, 76, 88 and 100 ms.

The longitudinal two-spin order rate $(R_{CH}(2H_zC_z))$ measurement starts with an INEPT-like step. This will, with suitable phase cycling, create the required population. After the delay τ, the longitudinal two-spin (dipolar)

order was converted to antiphase coherence and allowed to evolve into in-phase magnetisation. Using the same procedure as in the $R_C(C_{x,y})$ measurement, the carbon magnetization was stored along the z-axis while the proton magnetization was scrambled with hard pulses during 2.5 ms. Compared to the original pulse sequence described by Peng and Wagner, this extra step helps to suppress A_2X spin systems (Burum and Ernst, 1980) in addition to the previously mentioned advantages. The pulse sequence ends, as usual, with a refocused INEPT.

138

The τ values used were 35.7, 71.4, 107.1, 142.8, 179.8, 214.2 and 250 ms.

The relaxation rate of the antiphase coherence $(R_{CH}(2H_zC_{x,y}))$ was measured with a pulse sequence similar to the previous one. The spin-lock was applied on-resonance with a single phase during τ, instead of the phase-altered version used by Peng and Wagner. The same procedure with a scramble pulse was used as in the $R_{CH}(2H_zC_z)$ experiment. The τ values used were 17.8, 35.7, 53.6, 71.4, 89.2, 107.2 and 125 ms.

The last experiment was the measurement of the proton longitudinal relaxation rate $(R_H(H_z))$. The pulse sequence starts with a ^{13}C filter. Protons bound to ^{13}C will be inverted, while the other protons stay along the positive z-axis. No first-order cross relaxation between protons should therefore occur. The proton and the carbon will cross relax each other, since the carbons are not decoupled during τ, but because the cross-relaxation rate as calculated from NOE and carbon T_1 is quite small, the nuclei are effectively decoupled from each other with their separate monoexponential decays. The only addition to the original pulse sequence described by Peng and Wagner is that water suppression using an on-resonance DANTE pulse train was used during the delay τ. The τ values used were 8.9, 30.6, 61.2, 91.8, 122.4, 153.1, 183.7 and 214.3 ms.
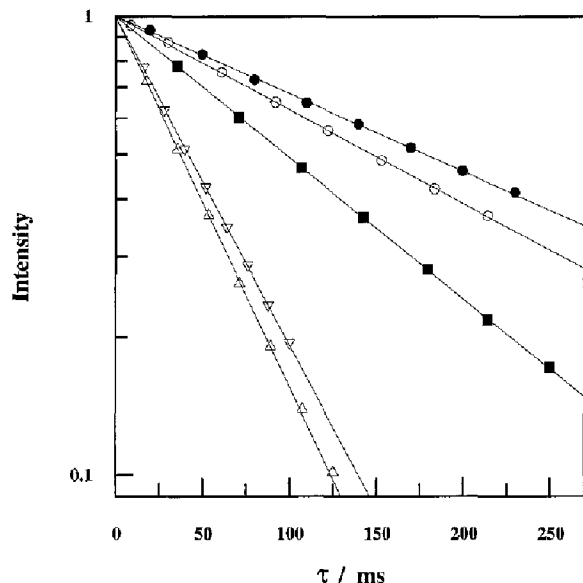

Fig. 2. Relaxation decays of five relaxation experiments at 30 °C for the $^{13}C^\alpha$-H$^\alpha$ vector in Leu[10] of motilin in 30% (v/v) HFP. (●) The carbon longitudinal relaxation decay, with the rate $R_C(C_z) = 3.89$ s^{-1}; (▽) the carbon in-phase transverse relaxation decay, with the rate $R_C(C_{x,y}) = 16.5$ s^{-1}; (■) the longitudinal two-spin order relaxation decay, with the rate $R_{CH}(2H_zC_z) = 7.08$ s^{-1}; (△) the antiphase coherence decay, with the rate $R_{CH}(2H_zC_{x,y}) = 18.6$ s^{-1}; and (○) the proton longitudinal relaxation decay, with the rate $R_H(H_z) = 4.69$ s^{-1}. All intensities are normalised to 1.0 for the fitted curve at $\tau = 0$. Experimental data are shown together with fitted single exponential decays $I(\tau) = I_0 \exp(-\tau R)$.

Data evaluation

Each free induction decay was zero-filled to 2048 points (resulting in a 1.95 Hz/pt digital resolution), multiplied with an exponential window of 15 Hz and Fourier transformed in magnitude mode. The maximum intensity of the spectrum was evaluated for each spectrum at a particular delay τ. Each experimental decay curve was fitted to a monoexponential function. The processing of NMR data was performed using FELIX software (Biosym Technologies, Inc.) and the fitting of decay curves was done using an external nonlinear Marquardt fitting routine (Press et al., 1988). Using the model-free approach (Lipari and Szabo, 1982a,b), the parameters τ_m, τ_e and S^2 were obtained by minimising the following target function:

$$\chi^2 = \sum_{i=1}^{3} (R_{exp}^i - R_{theor}^i)^2$$

with $R^i = [R_C(C_z), R_C(C_{x,y}), \{^1H\}-^{13}C$ NOE] and employing the simplex method (Nedler and Mead, 1965). The starting values used were: $\tau_m = 3$ ns, $\tau_e = 50$ ps and $S^2 = 0.9$. As three experimental values were fitted with three adjustable parameters, the model was able to fit exactly all three experimental values, and the relative weighting of relaxation data has no effect on fitted parameters. For fitting of the spectral density functions to the experimentally mapped spectral densities, the Grafit software (Erithacus Software Ltd., London) was applied, using explicit weighting based on the experimentally determined uncertainties.

Results and Discussion

Relaxation rates

A typical set of five relaxation decay curves at 30 °C for motilin in 30% (v/v) HFP are shown in Fig. 2. All experimental data fitted well with a single exponential decay $I(\tau) = I_0 \exp(-\tau R)$ and no systematic deviations were found. With at least seven experimental points, the average rmsd between these points and the fitted decay curve ranged from less than 0.5%, for $R_C(C_z)$ and $R_C(C_{x,y})$, to about 1% for $R_{CH}(2H_zC_{x,y})$ and $R_H(H_z)$.

The temperature dependences of the relaxation rates were analysed in order to estimate the random error in a way that is independent of decay fitting. Figures 3A and B show the relaxation rates evaluated at different temperatures in 30% (v/v) HFP and in pure D_2O, respectively. All temperature dependences of the decay rates are smooth and could be well approximated by second-order polynomials of the form $R(t) = k_0 + k_1 t + k_2 t$ for motilin in D_2O and by exponential dependences of the form $R(t) = k_0 + k_1 \exp(-t k_2)$ for motilin in 30% (v/v) HFP solution. This method of fitting the temperature dependences makes it possible to estimate the random errors in decay rates. These errors, estimated as mean values of random deviations of observed points from the fitted curves were: $R_C(C_z)$: 1.7%; $R_C(C_{x,y})$: 1.3%; $R_{CH}(2H_zC_{x,y})$: 2.7%;
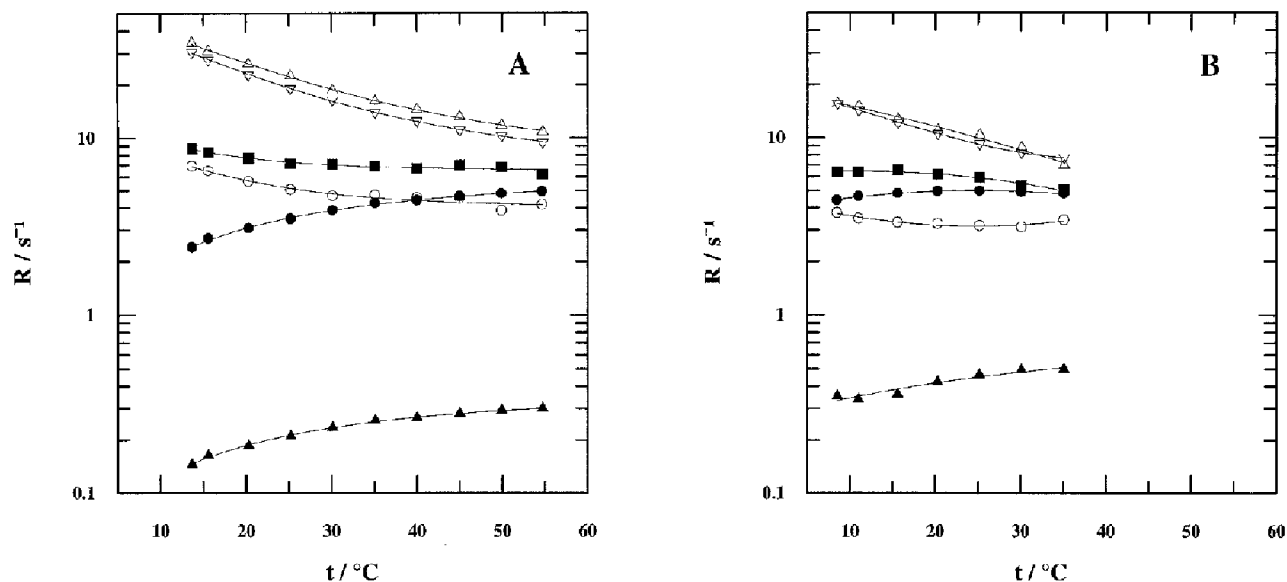
Fig. 3. The relaxation rates as functions of temperature for the ^{13}C-labelled α-carbon C^{α}-H^{α} vector of Leu^{10} in motilin: (A) in 30% (v/v) HFP and (B) in D_2O. (●) The carbon longitudinal relaxation rate $R_C(C_z)$; (▽) the carbon in-phase transverse relaxation rate $R_C(C_{x,y})$; (■) the relaxation rate of longitudinal two-spin order $R_{CH}(2H_zC_z)$; (△) the relaxation rate of antiphase coherence $R_{CH}(2H_zC_{x,y})$; (○) the proton longitudinal relaxation rate $R_H(H_z)$; and (▲) the heteronuclear cross-relaxation rate $R_{CH}(H_z \rightarrow C_z)$. Curves represent the best fit of relaxation rates to data in (A) using exponentials, and to data in (B) using second-order polynomials, as described in the text.

$R_{CH}(2H_zC_z)$: 2.3%; $R_H(H_z)$: 3.7%; and $R_C(H_z \rightarrow C_z)$: 10%. The difference in the temperature dependence of decay rates in different solvents is most evident for $R_C(C_z)$, which has a dependence with a maximum in D_2O (Fig. 3B), whereas in HFP no maximum is observed in the investigated temperature interval (Fig. 3A).

Five of the relaxation rates needed for spectral density mapping were measured directly. The sixth, the cross-relaxation rate $R_C(H_z \rightarrow C_z)$ between proton and carbon, was calculated from $R_C(C_z)$ and the steady-state $\{^1H\}$-^{13}C NOE using the following relation:

$$NOE = 1 + \frac{\gamma_H}{\gamma_C} \frac{R_C(H_z \rightarrow C_z)}{R_C(C_z)} \quad (1)$$

Here γ_H and γ_C are the gyromagnetic ratios for ^1H and ^{13}C, respectively. No systematic trend in the NOE intensities was observed over the investigated temperature range for the sample in 30% (v/v) HFP; an average NOE of 1.24 was used in all calculations. The cross-relaxation rate is the slowest of the measured rates by an order of magnitude. For the D_2O sample the NOE was temperature-dependent and changed from 1.30 at 15 °C to 1.41 at 35 °C.

Spectral densities

The spectral densities at each temperature were calculated from the six different relaxation rates using the relationship (Peng and Wagner, 1992a):

$$
\begin{bmatrix}
J(0) \\
J(\omega_C) \\
J(\omega_H - \omega_C) \\
J(\omega_H) \\
J(\omega_H + \omega_C) \\
\rho_{H^{\alpha}H'}
\end{bmatrix}
=
\begin{bmatrix}
-\dfrac{1}{8d} & \dfrac{1}{4d} & \dfrac{1}{4d} & -\dfrac{1}{8d} & -\dfrac{1}{8d} & 0 \\
\dfrac{1}{6d} & 0 & 0 & \dfrac{1}{6d} & -\dfrac{1}{6d} & 0 \\
\dfrac{1}{4d} & 0 & 0 & -\dfrac{1}{4d} & \dfrac{1}{4d} & -\dfrac{1}{2d} \\
-\dfrac{1}{12d} & \dfrac{1}{6d} & -\dfrac{1}{6d} & \dfrac{1}{12d} & \dfrac{1}{12d} & 0 \\
\dfrac{1}{24d} & 0 & 0 & -\dfrac{1}{24d} & \dfrac{1}{24d} & \dfrac{1}{12d} \\
-\dfrac{1}{4} & -\dfrac{1}{2} & \dfrac{1}{2} & \dfrac{1}{4} & \dfrac{1}{4} & 0
\end{bmatrix}
\times
\begin{bmatrix}
R_C(C_z) \\
R_C(C_{x,y}) \\
R_{CH}(2H_zC_{x,y}) \\
R_{CH}(2H_zC_z) \\
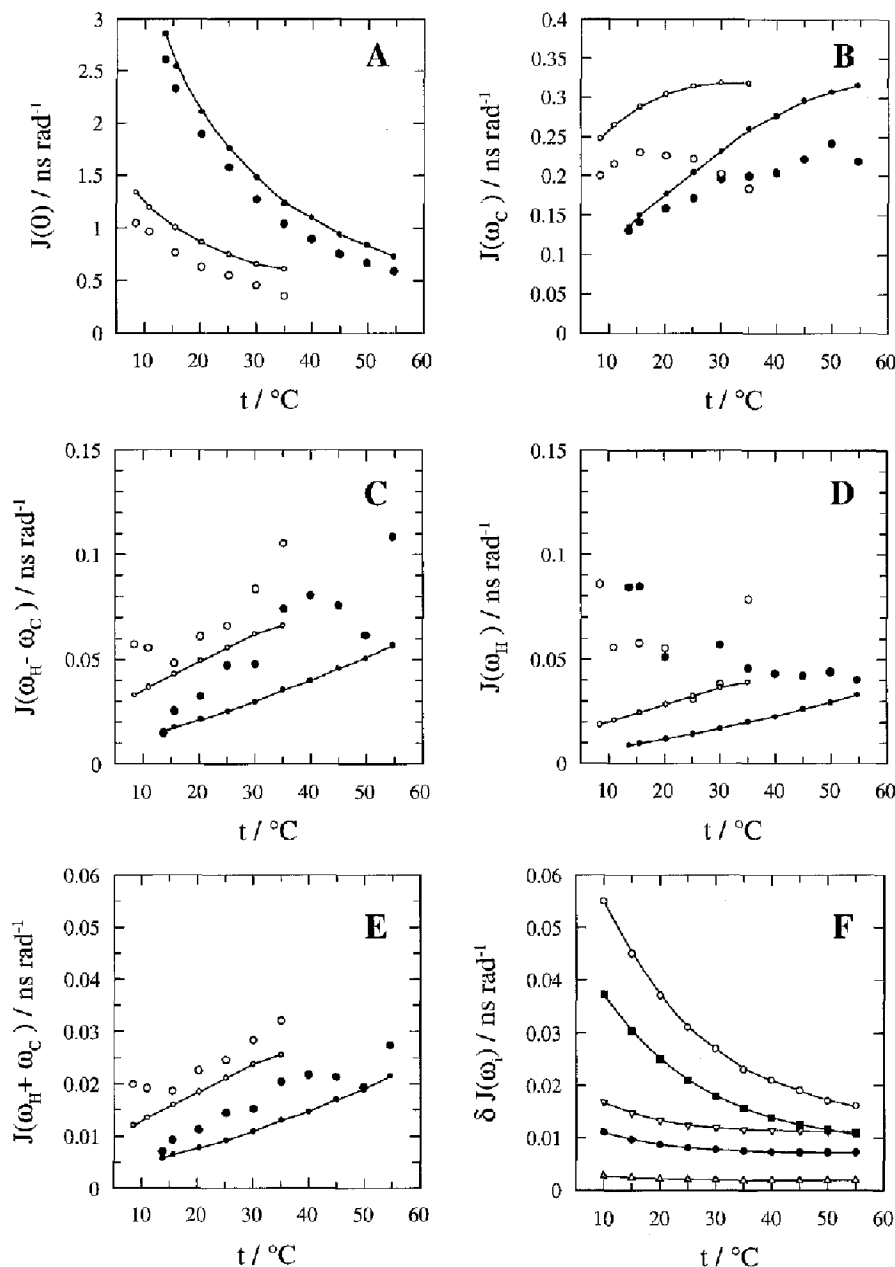R_H(H_z) \\
R_C(H_z \rightarrow C_z)
\end{bmatrix}
\quad (2)
$$

Fig. 4. Temperature dependence of the spectral densities (A) J(0); (B) J(100); (C) J(300); (D) J(400); and (E) J(500), for the vector connecting C^α and H^α of Leu[10] in motilin: (O) in D_2O and ($\bullet$) in 30% (v/v) HFP. Solid curves with smaller symbols represent spectral densities defined by the model-free spectral density function of Eq. 6, obtained in a classical way, i.e. using measured ^{13}C T_1, T_2 and NOE. Panel (F) shows the random errors in spectral densities $\delta J(\omega_i)$, estimated from uncertainties in relaxation rates in 30% (v/v) HFP using Eq. 4: (O) $\delta J(0)$; ($\bullet$) $\delta J(100)$; (∇) $\delta J(300)$; ($\blacksquare$) $\delta J(400)$; ($\triangle$) $\delta J(500)$. Note that in panel D the spectral density values in the two solvents are coinciding at 25 °C.

where

$$d = \frac{\gamma_H^2 \gamma_C^2 \hbar^2}{4r_{CH}^6} \qquad (3)$$

and $\rho_{H\alpha H i}$ is the α-proton longitudinal relaxation rate caused by other protons. The values of the constants used in Eqs. 2 and 3 are the following: $\gamma_H = 2.6752 \times 10^4$ rad s^{-1} $G s^{-1}$, $\gamma_C = 6.728 \times 10^3$ rad s^{-1} $G s^{-1}$, $\hbar = 1.0546 \times 10^{-27}$ erg s, $r_{CH} = 1.09$ Å, $d = 0.537 \times 10^{10}$ rad^2 s^{-2}.

Figure 4 shows the calculated spectral densities as a function of temperature in 30% (v/v) HFP and in D_2O.

The spectral densities are mainly affected by overall mobility, but toward higher temperatures the contribution from internal mobility increases. The zero-frequency spectral density J(0) has the largest amplitude and decreases rapidly with increasing temperature, while the high-frequency spectral densities in general increase with increasing temperature. This behaviour is expected, because the integral for the spectral density over frequency is constant (Abragam, 1962). A reduction of the low-frequency spectral density necessarily means that the high-frequency components must increase. Figure 4F

shows the random errors $\delta J(\omega_i)$ of the spectral densities, as defined by Peng and Wagner (1992a):

$$(\delta J(\omega_i))^2 = \sum_{j=1}^{6} c_{ij}^2 (\delta R_j)^2 \qquad (4)$$

where δR_j are the experimentally determined uncertainties from the temperature dependence of the relaxation rates and c_{ij} are the matrix elements in Eq. 2. The zero-frequency spectral density for the D_2O sample is less than one third of that for the 30% (v/v) HFP sample. It also decreases with increasing temperature. This behaviour can be understood, since the effective rotational correlation time is much smaller in aqueous solvent (see below) and this causes the zero-frequency spectral density to be correspondingly smaller.

The spectral densities at 100, 300 and 500 MHz have major contributions from three rates of similar sizes, two with positive signs and one with a negative sign. The resulting values of the spectral densities are therefore numerically well defined.

The 100 MHz spectral density (Fig. 4B) has about the same intensity in both solvents at room temperature, but becomes smaller with increasing temperature in the D_2O sample, while it increases in the 30% (v/v) HFP sample. The changes in dynamics with increasing temperature obviously occur at different time scales in the two cases.

It was found that the 400 MHz spectral density $J(\omega_H)$ is very sensitive to errors in relaxation rates and that the absolute errors are of the same magnitude as the absolute values of the spectral densities (cf. Figs. 4D and F). This is due to the fact that $R_C(C_{x,y})$ and $R_{CH}(2H_zC_{x,y})$ contribute to this spectral density by opposite signs. As these rates have the largest numerical values, the small difference is poorly defined and the random error may underestimate the true uncertainty for this spectral density. The 400 MHz spectral density should therefore be used with caution.

We can now discuss the relaxation rates based on the known spectral densities. The relaxation rates are related to the spectral densities through a linear system of equations, Eq. 5:

$J(0)$ is larger than any other of the mapped spectral densities, in most cases by an order of magnitude. It has a dominating effect on the transverse-type relaxation rates, $R_C(C_{x,y})$ and $R_{CH}(2H_zC_{x,y})$, which hence are the fastest rates. For $R_C(C_z)$ and $R_{CH}(2H_zC_z)$, where $J(0)$ is not contributing, the next lowest frequency spectral density, $J(\omega_C)$, dominates. Since $J(0)$ decreases with increasing temperature, the relaxation rates which include $J(0)$ will also decrease with increasing temperature.

Dynamics

From the results obtained in relaxation experiments we have determined a sufficient number of relaxation rates to enable evaluation of the spectral densities at five frequencies. This spectral density mapping has been done in two solvents, D_2O and 30% (v/v) HFP, at several temperatures in the intervals 8–36 °C and 13–55 °C, respectively. We have also analysed how the determined spectral densities contribute to the various relaxation rates. We will now examine how different models of the dynamics of the molecular fragment under study, the C^α-H^α vector of Leu[16] in porcine motilin, may fit with or explain the various spectral density maps. In all models to be discussed, it is assumed that the overall motion of the molecule is isotropic.

Isotropic rotation

This is the simplest model, in which only isotropic global motion is considered and local dynamics is supposed to be restricted to such an extent that it may be neglected. With this model, only the spectral density values obtained in 30% (v/v) HFP at low temperatures are reasonably well explained.

The model-free approach

Using the two experimental rates $R_C(C_z)$ and $R_C(C_{x,y})$ and the steady-state NOE, we applied the model-free approach (Lipari and Szabo, 1982a,b) to fit the spectral density function, Eq. 6:

$$
\begin{bmatrix}
R_C(C_z) \\
R_C(C_{x,y}) \\
R_{CH}(2H_zC_{x,y}) \\
R_{CH}(2H_zC_z) \\
R_H(H_z) \\
R_C(H_z \rightarrow C_z)
\end{bmatrix}
=
\begin{bmatrix}
0 & 3d & d & 0 & 6d & 0 \\
2d & \dfrac{3d}{2} & \dfrac{d}{2} & 3d & 3d & 0 \\
2d & \dfrac{3d}{2} & \dfrac{d}{2} & 0 & 3d & 1 \\
0 & 3d & 0 & 3d & 0 & 1 \\
0 & 0 & d & 3d & 6d & 1 \\
0 & 0 & -d & 0 & 6d & 0
\end{bmatrix}
\times
\begin{bmatrix}
J(0) \\
J(\omega_C) \\
J(\omega_H - \omega_C) \\
J(\omega_H) \\
J(\omega_H + \omega_C) \\
\rho_{H^\alpha H^i}
\end{bmatrix}
\qquad (5)
$$
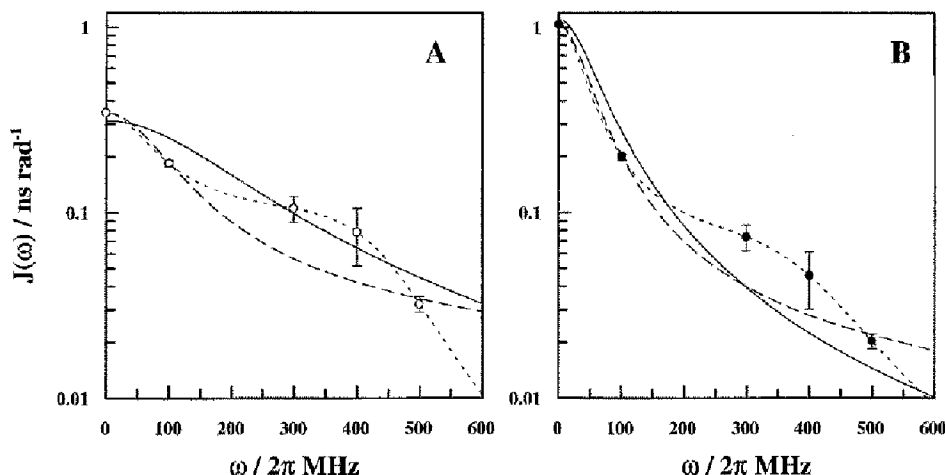
Fig. 5. Spectral density values, calculated from experimental relaxation rates using $r_{CH} = 1.09$ Å, for the $^{13}C^\alpha$-H^α vector in Leu[10] of motilin at 35 °C as functions of frequency (in MHz) in (A) D_2O and (B) 30% (v/v) HFP. The five sampling frequencies are 0, 100.49, 299.17, 399.66 and 500.14 MHz. In (A) the spectral density values for these frequencies are, in increasing frequency order: 0.345 ± 0.08, 0.183 ± 0.07, 0.105 ± 0.015, 0.078 ± 0.03 and 0.032 ± 0.003 ns rad^{-1}. In (B) the spectral density values are: 1.03 ± 0.02, 0.20 ± 0.008, 0.074 ± 0.01, 0.046 ± 0.015 and 0.020 ± 0.001 ns rad^{-1}. The solid curve represents the best fit to an isotropic rotation spectral density function with (A) $\tau_m = 0.78$ ns and (B) $\tau_m = 2.8$ ns. The dashed curve represents the best fit to a model-free approach spectral density function with parameters (A) $\tau_m = 1.6$ ns, $\tau_e = 140$ ps and $S^2 = 0.50$; and (B) $\tau_m = 3.4$ ns, $\tau_e = 180$ ps and $S^2 = 0.76$. The dotted curve corresponds to the spectral density function of Eq. 12 multiplied with a scaling factor f with the following parameters: (A) $\tau_m = 2.12$ ns, $\tau_e = 420$ ps, $S^2 = 0.41$, f = 0.72 and $\beta = 9.1$; and (B) $\tau_m = 3.9$ ns, $\tau_e = 420$ ps, $S^2 = 0.70$, f = 0.89 and $\beta = 7.0$.

$$J(\omega) = \frac{2}{5}\left[\frac{S^2\tau_m}{1+(\omega\tau_m)^2} + \frac{(1-S^2)\tau_i}{1+(\omega\tau_i)^2}\right] \quad (6)$$

with

$$\frac{1}{\tau_i} = \frac{1}{\tau_m} + \frac{1}{\tau_e} \quad (7)$$

The parameters used in this model are the overall rotational correlation time τ_m, the internal mobility correlation time τ_e and the order parameter S. S^2 and $(1 - S^2)$ are the amplitudes of the corresponding time-correlation functions. Since a total of three unknown parameters describe the motion, only three measurements are necessary to calculate these parameters. The three parameters describe the molecular motion for the vector along the bond between the carbon and hydrogen atoms. The correlation time τ_e for the fast internal motion cannot be interpreted directly and a dynamic model is therefore necessary. (One such dynamic model, similar to the model-free approach, is the so-called 'wobbling in a cone' model (Kinosita et al., 1977; Lipari and Szabo, 1980,1982a,b).)

The rotational correlation time τ_m (Eq. 6) in 30% (v/v) HFP decreases from 7 ns at 10 °C to 2 ns at 55 °C. This follows the decrease of viscosity with temperature. The square of the order parameter, S^2, decreases over the same temperature interval from 0.95 to 0.85. The time-correlation function is close to monoexponential at low temperatures and the large value of S^2 shows that the internal motion is highly restricted, even at high temperatures. Large order parameters are an indication of ordered structure, even though they cannot be used for differentiation between different kinds of secondary structure.

The internal correlation time τ_e decreases from 100 to 10 ps over the temperature interval. The two motions are on separate time scales and therefore statistically independent, as required by the model-free approach.

The rotational correlation time for motilin in D_2O, calculated using the model-free approach, changes from $\tau_m = 2.5$ ns at 15 °C to $\tau_m = 1.5$ ns at 35 °C. These values are compatible with the lower viscosity of D_2O compared to the mixed solvent. S^2 reduces from 0.82 to 0.70 in the same temperature interval.

Comparing these results with other applications of the model-free approach, we note that the average τ_e for backbone α-carbon nuclei in a zinc finger DNA-binding peptide Xfin-31 (Palmer et al., 1991) was evaluated as 34 $\pm$ 16 ps at 30 °C which, within error limits, is the same as our result of approximately 50 ps at the same temperature in both solvents.

Figures 5A and B show fitting of the isotropic rotation and the model-free approach spectral density functions to the five mapped spectral density points at 35 °C for motilin in D_2O and in 30% (v/v) HFP, respectively. From the fitting of a single correlation time spectral density function to the calculated spectral density data for D_2O and for 30% (v/v) HFP, we obtained $\tau_m = 0.78$ ns and $\tau_m = 2.8$ ns, respectively. The fitted values for the model-free spectral density function are: $\tau_m = 1.6$ ns, $\tau_e = 140$ ps and $S^2 = 0.50$ in D_2O and $\tau_m = 3.4$ ns, $\tau_e = 180$ ps and $S^2 = 0.76$ in 30% (v/v) HFP. It is obvious that neither model can fit the high-frequency points satisfactorily.

Three-step model

We have also considered what could be called the

three-step model, which includes four or five parameters. This model was introduced by Clore et al. (1990), because the model-free approach failed to account for relaxation data from several residues in staphylococcal nuclease and interleukin-1β. The three motions, characterised by the correlation times τ_m, τ_s and τ_f, should be time scale separated. The two high-frequency components correspond to the order parameters S_s and S_f, respectively, with $S^2 = S_s^2 S_f^2$. The spectral density function in this model is:

$$J(\omega) = \frac{2}{5}\left[\frac{S^2\tau_m}{1+(\omega\tau_m)^2} + \frac{(S_f^2-S^2)\tau_s'}{1+(\omega\tau_s')^2} + \frac{(1-S_f^2)\tau_f'}{1+(\omega\tau_f')^2}\right] \quad (8)$$

with

$$\frac{1}{\tau_f'} = \frac{1}{\tau_m} + \frac{1}{\tau_f} \quad (9)$$

$$\frac{1}{\tau_s'} = \frac{1}{\tau_m} + \frac{1}{\tau_s} \quad (10)$$

If $\tau_f < 10$ ps, the term containing τ_f may be neglected and only four parameters need to be fitted. The spectral density function reduces to (Clore et al., 1990):

$$J(\omega) = \frac{2}{5}S_f^2\left[\frac{S_s^2\tau_m}{1+(\omega\tau_m)^2} + \frac{(1-S_s^2)\tau_s'}{1+(\omega\tau_s')^2}\right] \quad (11)$$

When treating S_s^2 as S^2, it is evident that fitting Eq. 11 to the mapped spectral densities $J(\omega_i)$ is equivalent to introducing a scaling factor in the model-free approach, cf. Eq. 6. The same result would be obtained by changing the value of the distance r_{CH} in Eq. 3. As mentioned above, the contribution to dipolar relaxation from neighbouring protons is equivalent to a decrease of r_{CH}. Hence, the effects of a reduced effective distance r_{eff} and of very rapid restricted local motion may not be separated.

Attempts were made to fit Eqs. 8 and 11 to the mapped spectral densities, but they were not more successful than with the model-free approach (data not shown).

Summary of models discussed so far

A single correlation time is sufficient for a reasonable fit to the calculated spectral densities at temperatures around 15 °C (data not shown). However, at all higher temperatures, as shown for 35 °C in Fig. 5, the model-free approach with three parameters fails to give a good fit at higher frequencies. The same is true for the three-step model with four or five parameters.

The deviations of the mapped spectral densities from the spectral density function obtained by the model-free approach from the three experimental parameters $R_C(C_z)$, $R_C(C_{x,y})$ and the NOE can be seen in Fig. 4. For J(0) and J(100), the deviations are always negative and for the three high-frequency spectral densities they are in general positive. The numerical value of the deviation ΔJ(0) (Fig. 4A) is almost independent of temperature, whereas in

relative terms it increases with increasing temperature. The deviations of J(100) (Fig. 4B) and J(300) (Fig. 4C) both increase with increasing temperature, but in different directions, showing that it is increasingly difficult at higher temperatures for the model-free approach to reproduce their ratio. For J(500) (Fig. 4E) the deviations are positive and essentially temperature independent. The deviation of J(400) (Fig. 4D) is positive and seems to decrease with increasing temperature, but this tendency is less clear than at the other frequencies because of large relative errors (cf. Fig. 4F).

We have also applied the model-free approach by adjusting its three parameters to give the best fit between the calculated spectral density curve and the five mapped spectral densities. This is also shown in Fig. 5. It was found that deviations remained which were similar to, but less accentuated than, those described above.

We therefore turn to consider possible additional relaxation mechanisms or relaxation pathways which will give too high apparent relaxation rates. Systematic errors in the experimental relaxation rates are propagated into the spectral densities, as shown by Eq. 2. One example is that both transverse relaxation rates $R_C(C_{x,y})$ and $R_{CH}(2H_zC_{x,y})$ may be influenced by conformational exchange. The only two spectral densities affected by these rates are J(0) and J(400). Assuming that both rates are overestimated by equal amounts, say 10% of $R_{CH}(2H_zC_{x,y})$, the correction in J(0) would be -14%. In J(400) the two corrections will have different signs and effectively cancel out. A second example is that another relaxation pathway may arise from homonuclear proton cross relaxation. In our case this would lead to overestimates of $R_{CH}(2H_zC_{x,y})$, $R_{CH}(2H_zC_z)$ and $R_H(H_z)$. Again, we assume that these rates are overestimated by the same amount. In J(100), J(300) and J(500) only the two latter rates enter, but the two corrections have opposite signs and cancel out. All three rates enter in J(0) and J(400), but in both cases the effect from the first rate will be balanced by the combined effect from the other two rates. In both of the above examples the shape of the J(ω) curve at high frequencies (particularly the slope between J(300) and J(500)) remains essentially unchanged. This shape could be affected by the type of relaxation pathways discussed only if there is a large unbalance between the efficiencies by which the respective pulse sequences are sampling the effect. However, such discriminating unbalances seem highly unlikely.

We interpret the deviations between the model-free spectral density function and our mapped spectral densities to indicate that several additional high-frequency processes are involved in the peptide dynamics, particularly at the higher temperatures applied. The dynamic models presently in use are not capable of incorporating this aspect, even if they still give useful information about the overall rotational correlation time τ_m and the order parameter S.

Frequency dependence of spectral densities

As is apparent from the previous discussion, the model-free approach needs modification in order to fit the experimental high-frequency spectral densities $J(\omega_H - \omega_C)$, $J(\omega_H)$ and $J(\omega_H + \omega_C)$. It was proposed that several additional high-frequency processes might be involved. Then, it would be natural to try to modify the spectral density function of the model-free approach in that direction. It was also found that a model with two time scale separated high-frequency components does not improve the situation. Hence, a distribution of high-frequency components should be attempted. In dielectric relaxation theory it has been proven useful to modify the Debye formula to account for a distribution of correlation times (Havriliak and Negami, 1967; Lindsey and Patterson, 1980). We have tried to use a similar formulation of the spectral density function $J(\omega)$, including a new parameter β:

$$J(\omega) = \frac{2}{5}\left[\frac{S^2\tau_m}{1+(\omega\tau_m)^2} + \frac{\beta}{2}\sin\left(\frac{\pi}{\beta}\right)\frac{(1-S^2)\tau_i}{1+(\omega\tau_i)^\beta}\right] \quad (12)$$

This spectral density function is normalised in the same way as the spectral density of the model-free approach. In dielectric relaxation theory, the parameter β is considered to correspond to a symmetric distribution of correlation times. The overall part of the model-free approach formula is unchanged, whereas the effective correlation time part is modified and normalised. The resulting spectral density function is purely empirical and does not correspond to any known motional model. It was pointed out by Lipari and Szabo (1982a) that simple models, containing only a few types of motion, lead to correlation functions containing a large number of spectral density components, and that the complete correlation function for the diffusion in the cone model has an infinite number of components. Nevertheless, when one considers a dynamic model for the time-correlation function $C(t)$, there should be a correspondence between the relevant parameter(s) of the time-correlation function and the parameter β in the spectral density function of Eq. 12.

In applying the spectral density function of Eq. 12 to the experimental data, we also include, in analogy with Eq. 11, a scaling factor f to be multiplied with the spectral density function of Eq. 12, to account for an adjustable effective distance. This new five-parameter function $fJ(\omega)$ could be fitted to the five experimentally determined values of Fig. 5, which gives the following parameters at 35 °C in D_2O: $\tau_m = 2.12$ ns, $\tau_e = 420$ ps, $S^2 = 0.41$, $\beta = 9.1$ and $f = 0.72$; and in 30% HFP: $\tau_m = 3.90$ ns, $\tau_e = 420$ ps, $S^2 = 0.70$, $\beta = 6.98$ and $f = 0.89$. The determined f-values are below 1 and translate into values of $r_{eff} > 1.09$ Å. Such large r_{eff} values seem unrealistic in view of our previous discussion. Also, the β-values are much larger than those used in the dielectric relaxation studies

(Havriliak and Negami, 1967; Lindsey and Patterson, 1980). A search for a theoretically based dynamics model, including a non-Lorentzian shape of the spectral density function, is nevertheless indicated.

Rotational diffusion

The overall rotational correlation time τ_m may now be estimated in various ways (see Table 1). The simplest way is to use the ratio between $R_C(C_z)$ and $R_C(C_{x,y})$ ($\tau_m = 5.2$ ns at 20 °C in 30% (v/v) HFP). It has been shown that this will give a reasonable estimate of τ_m, because the deviations caused by internal mobility will partially cancel (Palmer et al., 1991; Redfield et al., 1992). These two relaxation experiments can also be performed using ^{13}C at natural abundance, by integrating the 1D spectra over all α-carbons (Arvidsson et al., 1994). A second possibility is to calculate τ_m from the model-free approach using $R_C(C_z)$, $R_C(C_{x,y})$ and steady-state NOE, which gave $\tau_m = 5.3$ ns. If all five spectral density points are utilised, the spectral density function of either the isotropic rotation model or the model-free approach can be used, yielding τ_m values of 4.7 and 5.4 ns, respectively.

Obviously, these four NMR methods give very similar results for τ_m, as is expected for cases where the order parameter is large. If information on fast dynamics is not needed, τ_m derived from the ratio of $R_C(C_z)$ to $R_C(C_{x,y})$ usually is sufficient.

The rotational correlation time of motilin in 30% (v/v) HFP has previously been measured using time-resolved fluorescence polarisation anisotropy decay (Backlund and Gräslund, 1992,1995). The measurements were performed using [Tyr7] as an intrinsic fluorescence probe. The most precise measurements in 30% HFP at various temperatures gave values of τ_m (Table 1) which are lower by about a factor of two compared to the present ^{13}C NMR relaxation results (Backlund et al., 1995). Similar deviations between results from ^{13}C NMR and fluorescence have been noted for a zinc finger peptide (Palmer et al., 1993) and thioredoxin (Kemple et al., 1994). Although systematic errors in the two types of measurements and the application of a motional model could influence the results, the different viscosities in a highly concentrated peptide/protein NMR solution and a dilute solution for fluorescence studies may contribute as well.

Proton NMR measurements using the ratio of cross-peak to diagonal-peak intensities in a NOESY spectrum have also been applied for estimation of the rotational correlation time of motilin (Khan et al., 1990). The crude approximation made in this case is that a single correlation time describes the motion, and this approach therefore gives only a lower limit of the real rotational correlation time.

We consider a large order parameter to be necessary for accurate determination of τ_m. It is very difficult to account for the influence from the internal motion if that

TABLE 1
τ_m AND S^2 FOR PORCINE MOTILIN DETERMINED USING DIFFERENT METHODS

Method	Model / data	Residue	τ_m (ns)	S^2
NMR	Isotropic rotation / T_1, T_2	Leu[10]	5.2	(1)
NMR	Model free / T_1, T_2 and NOE	Leu[10]	5.3	0.93
NMR	Isotropic rotation / five spectral density points	Leu[10]	4.7	(1)
NMR	Model free / five spectral density points	Leu[10]	5.4	0.87
TFD[a]	Two τ_m values / anisotropy decay	Tyr[7]	2.2	0.38[b]

τ_m = rotational correlation time; S^2 = squared order parameter. The parameters were determined in 30% (v/v) HFP at 20 °C. In the case of isotropic rotation, $S^2 = 1$ by definition (indicated in parentheses).
[a] From fluorescence polarisation anisotropy decay studies (Backlund et al., 1995).
[b] The TFD order parameter was calculated as a ratio of fluorescence anisotropy decay component amplitudes $S^2 = \beta_2 / (\beta_1 + \beta_2)$.

motion has a significant amplitude. This difficulty applies to both fluorescence decay and NMR relaxation studies.

The activation energy of the rotational motion could be calculated using the Arrhenius relation. With τ_m from the model-free approach, we obtain the activation energy $E_A = 6.0$ kcal/mol for motilin in 30% (v/v) HFP. For motilin in water the corresponding activation energy is 4.6 kcal/mol. From the fluorescence studies, a corresponding value of E_A was found to be 6.1 kcal/mol for motilin in 30% (v/v) HFP (Backlund et al., 1995), in good agreement with NMR results. These figures are close to the activation energies of the viscosities for the solvents in this temperature range (data not shown).

The longitudinal and transverse relaxation rates of the ^{13}C α-carbon of Leu[10] were also determined for a 20 times diluted sample of motilin in 30% (v/v) HFP. This gave an overall rotational correlation time that was 15% smaller than in the concentrated sample. The errors in the relaxation rates with 0.32 mM motilin were about five times larger than in the rates measured at 7.1 mM concentration. It may be concluded that no significant changes in aggregation state or solvation occur in the concentration interval studied. The observed effect could be due to the viscosity contribution of the peptide itself.

Conclusions

We have shown that, using ^{13}C labelling and ^{13}C NMR with inverse detection, it is possible to measure relaxation rates of the C^α-H^α vector and to map the spectral density function with high precision.

Six relaxation rates were measured. From these the spectral densities could be calculated at five frequencies. For a C^α-H^α coupled system and using a 9.4 T polarising magnetic field, those frequencies are 0, 100.49, 299.17, 399.66 and 500.14 MHz. The data are distributed rather uniformly on the frequency scale. At the same time, when considering the corresponding characteristic correlation times, i.e. ω^{-1}, it is evident that these times are clustered in the time region 0.3–2 ns.

The frequency and temperature dependence of spectral densities of motilin are complex. Residue Leu[10], with the

^{13}C α-carbon label, is in a helix which is relatively stable in 30% (v/v) HFP over the whole temperature range. In the D_2O sample, the label is in a less ordered structure. The zero-frequency spectral densities are of much lower intensity in this case. Both the model-free approach with three parameters and the three-step model with four to five parameters fail to account for the frequency dependence of the high-frequency components observed with spectral density mapping.

The model-free approach is appropriate to separate the overall and average internal mobilities. It is apparent that a good fit to the experimental high-frequency spectral density points obtained here would require some modification of the approach, including an extra parameter.

The ^{13}C nucleus is in several respects more suitable for spectral density mapping than ^{15}N. The spectral density is more evenly mapped because the Larmour frequency for ^{13}C is close to one third of the proton frequency, whereas the ^{15}N frequency is much smaller. Water suppression and proton exchange are also less of a problem when using ^{13}C. By using a single label, or just a few labels, in a peptide it is possible to use 1D instead of 2D experiments. This reduces the time required for a complete set of experiments and makes it easier to study temperature and solvent effects. Such spectral density mapping is done advantageously using a relatively weak magnetic field. Sensitivity is not a serious problem and the numerical values of the spectral densities at different frequencies will be of more uniform size.

The frequency range is easily extended by using different polarising fields. For peptides, the lower fields will be more informative as the sampling points fall on the decay slope of the spectral density function, which is the sensitive part to high-frequency mobility components. However, also the present results, using only one polarising field, give unique information about the overall mobility as well as the internal dynamics of the peptide.

Acknowledgements

References

Abragam, A. (1962) *The Principles of Nuclear Magnetism,* 2nd ed., Clarendon Press, Oxford, pp. 264–323.

Arvidsson, K., Jarvet, J., Allard, P. and Ehrenberg, A. (1994) *J. Biomol. NMR,* **4**, 653–672.

Backlund, B.-M. and Gräslund, A. (1992) *Biophys. Chem.,* **45**, 17–26.

Backlund, B.-M., Wikander, G., Peeters, T.L. and Gräslund, A. (1994) *Biochim. Biophys. Acta,* **1190**, 337–344.

Backlund, B.-M., Kulinsky, T., Rigler, R. and Gräslund, A. (1995) *Eur. Biophys. J.,* in press.

Barbato, G., Ikura, M., Kay, L.E., Pastor, R.W. and Bax, A. (1992) *Biochemistry,* **31**, 5269–5278.

Burum, D.P. and Ernst, R.R. (1980) *J. Magn. Reson.,* **39**, 163–168.

Clore, G.M., Szabo, A., Bax, A., Kay, L.E., Driscoll, P.C. and Gronenborn, A.M. (1990) *J. Am. Chem. Soc.,* **112**, 4989–4991.

Daragan, V.A. and Mayo, K.H. (1992) *J. Am. Chem. Soc.,* **114**, 4326–4331.

Edmondson, S., Khan, N., Shriver, J., Zdunek, J. and Gräslund, A. (1991) *Biochemistry,* **30**, 11271–11279.

Havriliak, S. and Negami, S. (1967) *Polymers,* **8**, 161–210.

Kay, L.E., Nicholson, L.K., Delaglio, F., Bax, A. and Torchia, D.A. (1992) *J. Magn. Reson.,* **97**, 359–375.

Kemple, M.D., Yuan, P., Nollet, K.E., Fuchs, J.A., Silva, N. and Prendergast, F.G. (1994) *Biophys. J.,* **66**, 2111–2126.

Khan, N., Gräslund, A., Ehrenberg, A. and Shriver, J. (1990) *Biochemistry,* **29**, 5743–5751.

Kinosita, K., Kawato, S. and Ikegami, A. (1977) *Biophys. J.,* **20**, 289–305.

Kondo, Y., Torii, K., Omura, S. and Itoh, Z. (1988) *Biochem. Biophys. Res. Commun.,* **150**, 877–882.

Kowalewski, J., Ericsson, A. and Vestin, R. (1978) *J. Magn. Reson.,* **31**, 165–169.

Lindsey, C.P. and Patterson, G.D. (1980) *J. Chem. Phys.,* **73**, 3348–3357.

Lipari, G. and Szabo, A. (1980) *Biophys. J.,* **30**, 489–506.

Lipari, G. and Szabo, A. (1982a) *J. Am. Chem. Soc.,* **104**, 4546–4559.

Lipari, G. and Szabo, A. (1982b) *J. Am. Chem. Soc.,* **104**, 4559–4570.

Morris, G.A. and Freeman, R. (1978) *J. Magn. Reson.,* **29**, 433–462.

Morris, G.A. and Freeman, R. (1979) *J. Am. Chem. Soc.,* **101**, 760–762.

Nedler, J.A. and Mead, R. (1965) *Comput. J.,* **7**, 308–313.

Palmer III, A.G., Rance, M. and Wright, P.E. (1991) *J. Am. Chem. Soc.,* **113**, 4371–4380.

Palmer III, A.G., Skelton, N.J., Chazin, W.J., Wright, P.E. and Rance, M. (1992) *Mol. Phys.,* **75**, 699–711.

Palmer III, A.G., Hochstrasser, R.A., Millar, D.P., Rance, M. and Wright, P.E. (1993) *J. Am. Chem. Soc.,* **115**, 6333–6345.

Peng, J.W., Thanabal, V. and Wagner, G. (1991) *J. Magn. Reson.,* **95**, 421–427.

Peng, J.W. and Wagner, G. (1992a) *J. Magn. Reson.,* **98**, 308–332.

Peng, J.W. and Wagner, G. (1992b) *Biochemistry,* **31**, 8571–8586.

Poitras, P. (1994) In *Gut Peptides: Biochemistry and Physiology* (Eds, Walsh, J.H. and Dockray, G.J.) Raven Press, New York, NY, pp. 261–304.

Press, W.H., Flannery, B.P., Teukolsky, S.A. and Vetterling, W.T. (1988) *Numerical Recipes. The Art of Scientific Computing,* Cambridge University Press, Cambridge, pp. 542–547.

Redfield, C., Boyd, J., Smith, L.J., Smith, R.A.G. and Dobson, C.M. (1992) *Biochemistry,* **31**, 10431–10437.

Rossi, C., Sansoni, M.R. and Donati, A. (1991) *Chem. Phys. Lett.,* **187**, 439–441.

Shaka, A.J., Keeler, J., Frankiel, T. and Freeman, R. (1983) *J. Magn. Reson.,* **52**, 335–338.

Sklenář, V., Torchia, D. and Bax, A. (1987) *J. Magn. Reson.,* **73**, 375–379.

Wetlaufer, D.B. (1962) *Adv. Protein Chem.,* **17**, 303–390.

Zuiderweg, E.R.P., Hallenga, K. and Olejniczak, E.T. (1986) *J. Magn. Reson.,* **70**, 336–343.